RANS Based CFD Methodology of Wire-wrapped Fuel Bundles

J. H. Jeong [a*], H. Y. Jeong [b], K. S. Ha [a]
[a] *Korea Atomic Energy Research Institute, 989-111, Daedeok-daero, Yuseong-gu, Daejeon, 305-353*
[b] *Sejong University, 209, Neungdong, Gwangjin-gu, Seoul, 143-747*
[*] *Corresponding author: jhjeong@kaeri.re.kr*

1. Introduction

SFR (Sodium-cooled Fast Reactor) system is one of the nuclear reactors in which a recycling of transuranics (TRUs) by reusing spent nuclear fuel sustains the fission chain reaction. This situation strongly motivated Korea Atomic Energy Research Institute (KAERI) to start a Prototype Gen-Ⅳ Sodium-cooled Fast Reactor (PGSFR) design project under the national nuclear R&D program. Generally, SFR system has tight package of the fuel bundle and the high power density. The fuel assembly of SFR system is consisted of wire-wrapped fuel bundles with triangular loose array. The bundles of the SFR fuel assembly usually consisted of rods and wire spacers. The main purpose of the wire is to avoid collision between adjacent rods. Furthermore, a vortex induced vibration can be mitigated by wire spacers. In this study, the RANS based CFD methodology using an innovative grid generation has been evaluated in the 7-pin, 37-pin, and 217-pin wire-wrapped fuel assembly, which is using the general-purpose commercial CFD code, CFX.

2. Numerical Analysis Methodology

The experimental study of the 7-pin [1] and 37-pin [2] fuel assembly was carried out in the sodium boiling and fuel failure propagation test loops (SIENA) installed at PNC's Oarai engineering center. The 2014 PGSFR fuel assembly was designed by KAERI.

2.1 Test Section of Numerical Analysis

Design specifications of the 7-pin, 37-pin, and 217-pin fuel assembly are summarized in Table 1, 2, and 3, respectively.

Table 1. Test section geometry parameters of 7-pin

Geometry parameters	Test section
Number of pins	7
Pin diameter (mm)	6.5
Pin pitch (mm)	7.9
Pin length (mm)	1317
Heated length (mm)	450
Heat flux distribution	Uniform
Tube flat-to-flat distance (mm)	23.6
Wire spacer diameter (mm)	1.1
Wire lead pitch (mm)	264.8

Table 2. Test section geometry parameters of 37-pin

Geometry parameters	Test section
Number of pins	37
Pin diameter (mm)	8.5
Pin pitch (mm)	9.65
Pin length (mm)	1650
Heated length (mm)	650
Heat flux distribution	Uniform
Tube flat-to-flat distance (mm)	60.94
Wire spacer diameter (mm)	1.1
Wire lead pitch (mm)	200

Table 3. Test section geometry parameters of 217-pin

Geometry parameters	Test section
Number of pins	217
Pin diameter (mm)	7.4
Pin pitch (mm)	8.436
Pin length (mm)	970
Heated length (mm)	900
Heat flux distribution	Non-uniform
Tube flat-to-flat distance (mm)	126.36
Wire spacer diameter (mm)	0.95
Wire lead pitch (mm)	199.6

2.2 Innovative Grid Generation Method

The computational grids system of the 7-pin, 37-pin, and 217-pin fuel assembly is composed of hexagonal meshes using the innovative grid generation methodology. Fig. 1 shows the cross sectional view of the CFD analysis. Fig. 2 shows the enlarged view of the

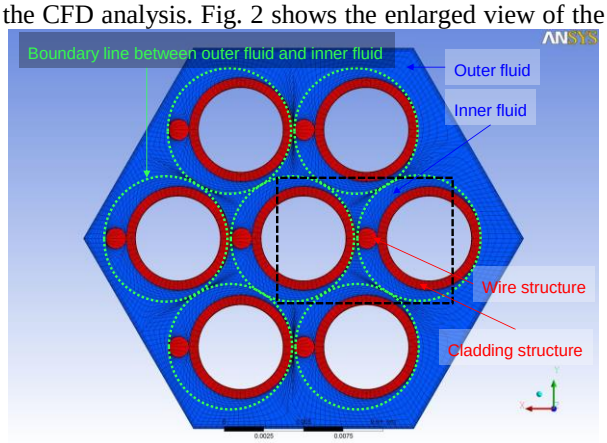

Fig. 1. Cross sectional view of the 7-pin fuel bundles

black dotted line of Fig. 1. As shown in Fig. 1 and Fig. 2, fuel bundle geometries such as the diameter of the rod and wire are fully simulated in this study. In the innovative grid generation methodology using in-house code, the boundary line (green dotted line) between the helically arranged meshes (inner fluid region) and straightly arranged meshes (outer fluid region) is adopted with General Grid Interface (GGI) function of the CFX code.

Table 4, 5, and 6 describe the computational grids system of the 7-pin, 37-pin, and 217-pin, respectively. Compared to other studies with trimmed shape [3~6], the number of meshes without any trimmed shape remarkably decreases as shown in table 4, 5, and 6.

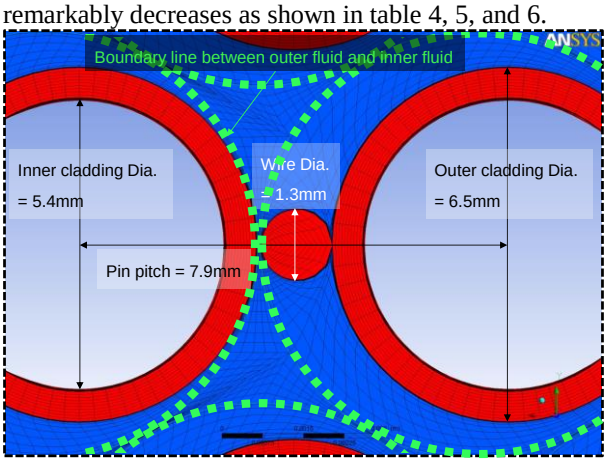

Fig. 2. Enlarged view of the 7-pin fuel bundles

Table 4. Computational grids system of 7-pin

7-Pin	Cells	Nodes	Elements
Sub-channels	1,467,200s	1,632,444	1,467,200
Cladding	550,200	619,080	550,200
Wire	77,028	97,020	77,028
Total	2,094,428	2,348,544	2,094,428

Table 5. Computational grids system of 37-pin

37-Pin	Cells	Nodes	Elements
Sub-channels	7,510,800	8,943,016	7,510,800
Cladding	1,862,025	2,142,266	1,862,025
Wire	512,820	590,001	512,820
Total	9,885,645	11,675,283	9,885,645

Table 6. Computational grids system of 217-pin

217-Pin	Cells	Nodes	Elements
Sub-channels	24,552,640	27,334,947	24,552,640
Cladding	6,314,700	7,030,282	6,314,700
Wire	1,768,116	1,968,479	1,768,116
Total	32,635,456	36,333,708	32,635,456

2.3 Boundary Conditions

Table 7 describes the computational boundary condition of the CFD analysis. As shown in table 7, inlet and outlet are defined with constant velocity of various values and relative pressure of 0 Pa, respectively. Rod outer and wire outer are defined with no slip condition and smooth roughness. Duct wall is applied to no slip and adiabatic condition.

Table 7. Boundary condition in helically wrapped 7-pin, 37-pin, 217-pin fuel assembly

Boundary domain	Condition	Value
-Inlet	-Constant velocity	Various
-Outlet	-Relative pressure	0 [Pa]
-Inner cladding (Heat source)	-Constant heat flux	Various
-Rod outer -Wire outer	-No slip -Smooth wall	-
-Duct Wall	-No slip -Adiabatic	-

2.4 Turbulence Model

Numerical simulation techniques of turbulent flow are typically divided into DNS (Direct Numerical Simulation), LES (Large Eddy Simulation), and RANS (Reynolds Averaged Navier-Stokes simulation). DNS resolves all range of spatial and temporal scales of the turbulence. Because the grid and time scales of DNS need to be less than Kolmogorov scale that is the smallest dissipative scales, the DNS requires fine grids and small time interval. LES solves spatially filtered Navier-Stokes equations on coarser grids. Thus, the LES does not resolve the entire scales of the turbulent flosw. LES resolves only large scales of the turbulent flow. Small scales of the turbulent flow are modeled using sub-grid scale (SGS) models by Smagorinsky [7]. RANS solves for time averaged Navier-Stokes equations and models the all scales of the turbulence using turbulence models such as k-ε, k-w, and SST.

Assuming that computing cost of the RANS is equal to be one, that of the DNS and LES increases as the cube and square of Reynolds number, respectively. Reynolds number based on the averaged axial velocity and the hydraulic diameter of the present fuel assembly is more than 1.00×10^4. For this reason, the DNS and LES are not feasible methods for the fuel assembly simulation. The RANS is very practical and affordable engineering solutions with good knowledge of the turbulence.

The turbulence models for the RANS equations are for computing the Reynolds stresses tensor from turbulent fluctuations in fluid momentum. The turbulence models like the k-ε, k-w, and SST have become industry standard models and are commonly used for most types

of engineering problems, although *k-ε* model has the weakness in cases of large adverse pressure gradient and *k-w* model is too sensitive to the inlet free-stream turbulence properties [8]. SST model solves above problems for switching to the *k-ε* model in the free-stream and the *k-w* model in the viscous sub-layer [9]. Minimum grid scale on the fuel rod wall surface was 5.0×10^{-7} mm to capture the laminar to turbulent flow transition with SST turbulence model; the friction velocity y* is approximately close to one.

2.5 Grid Sensitivity Study

To save computational time, the sensitivity study of the wall y* grid scale is carried out using the wire-wrapped 7-pin fuel assembly. Fig. 3 shows the friction factor with different wall grid scale in the wire-wrapped 7-pin fuel assembly. As shown in Fig. 3, friction factor uncertainties with the different wall grid spacing in CFD simulation with SST turbulence model was under the 6.0 %.

Validation of the GGI function has been carried out by comparison of the CFD analysis results with GGI mesh with the CFD analysis results with 1:1 mesh along the boundary line in Fig. 2. As shown in Fig. 4 and 5, both of axially distributed area-averaged bulk temperature and line-averaged wall temperature have almost same value. The axial maximum bulk and wall temperature difference between 1:1 mesh and GGI mesh is described in Table 8.

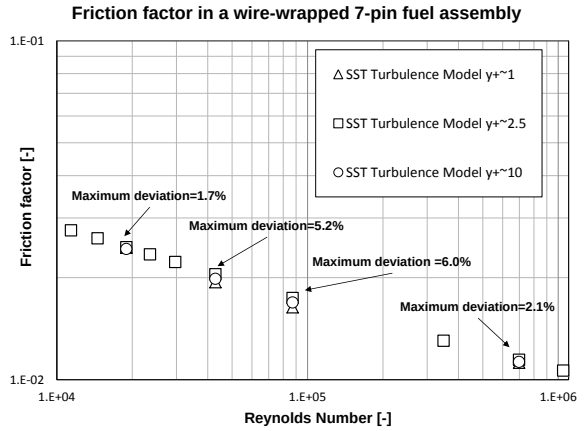

Fig. 3. Friction factor with different wall grid scale

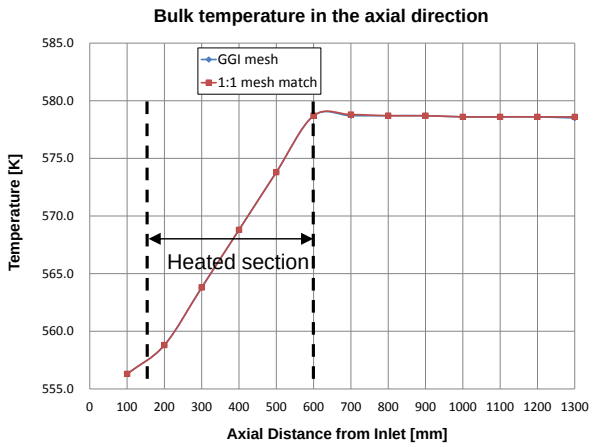

Fig. 4. Axially distributed area-averaged bulk temperature

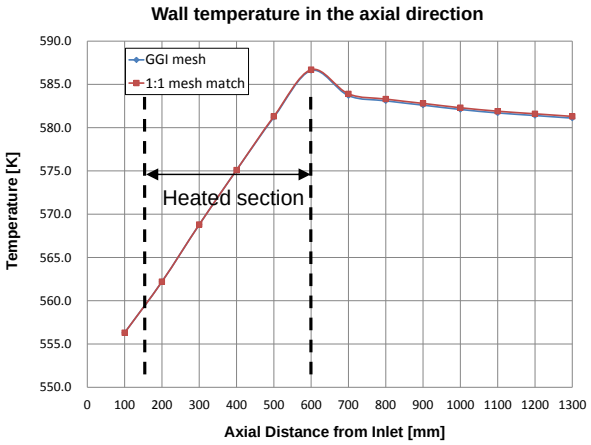

Fig. 5. Axially distributed line-averaged wall temperature

Table 8. Axial maximum bulk and wall temperature difference between GGI mesh and 1:1 mesh

Variables	Maximum difference
Bulk temperature [℃]	0.1
Wall temperature [℃]	0.2

2.6 Review of Calculated Variables

Fig. 6, 7, 8, and 9 show the pressure, normalized velocity by the inlet velocity, temperature, and density distribution of downstream view on the cross sectional plane of Z=530mm from inlet region. As shown in Fig. 6, the wires are rotating counter-clockwise from downstream view. As the wires are helically wrapped in the axial direction, the complicated pressure and velocity field are formed in Fig. 6 and 7. As shown in Fig. 7, the axial velocity in the corner and edge sub-channels is higher than that in the interior sub-channels. However, the tangential velocity due to wires is closely related the relative position between the wire and duct wall surface. These complicated and vortical flow fields decide the temperature field in Fig. 8. As shown in Fig.

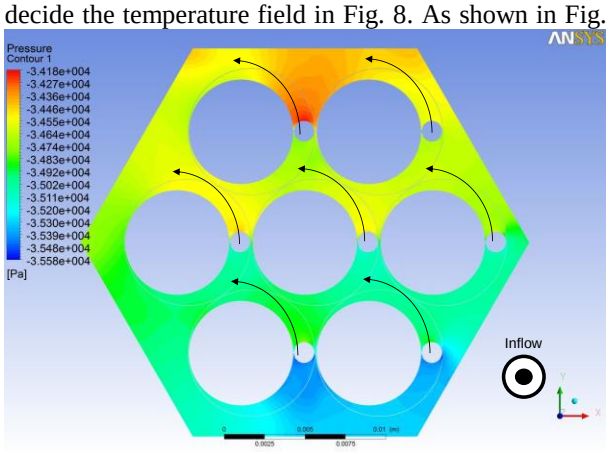

Fig. 6. Pressure distribution from downstream view

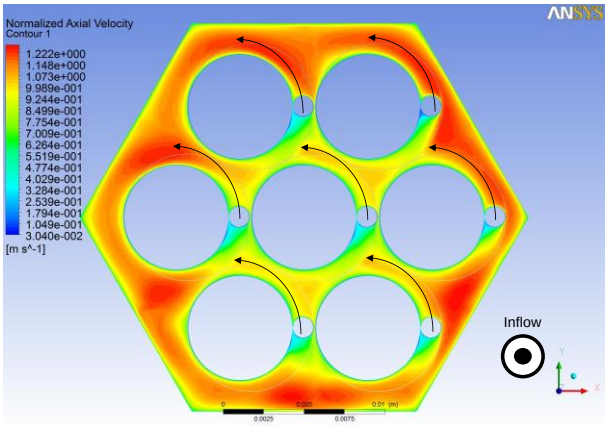

(a) Normalized axial velocity by inlet velocity

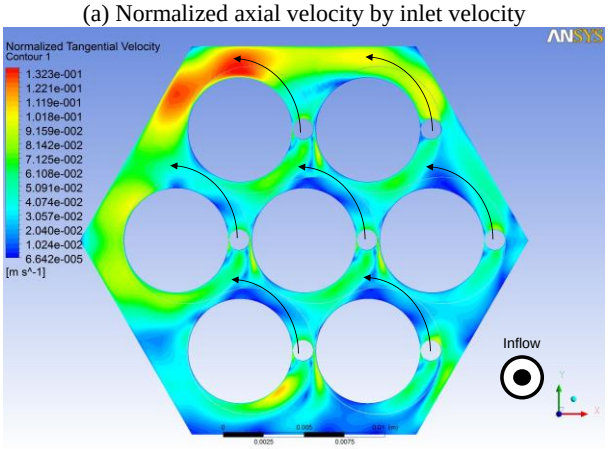

(b) Normalized tangential velocity by inlet velocity

Fig. 7. Velocity distribution from downstream view

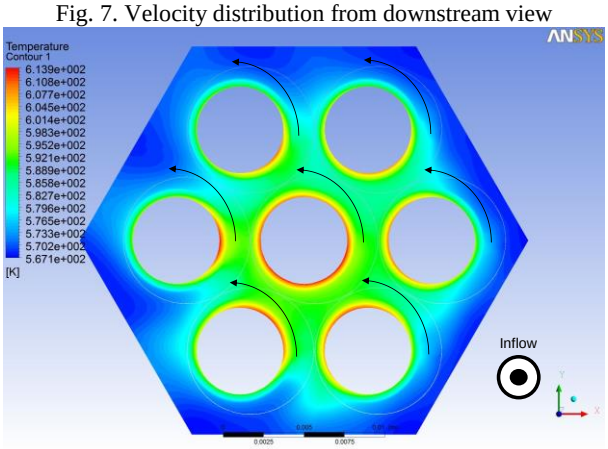

Fig. 8. Temperature distribution from downstream view

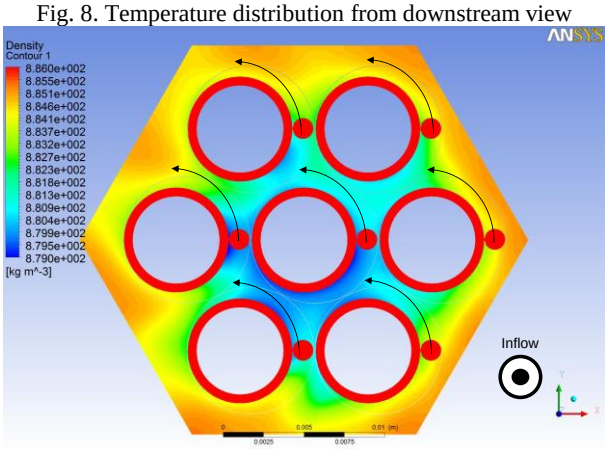

Fig. 9. Density distribution from downstream view

9, the density of the sodium changes with only temperature in this RANS based CFD methodology.

3. Extended Numerical Analysis Results

This section provides a review of the RANS based CFD analysis results of the various fuel assemblies of 7-pin, 37-pin, and 217-pin. Many efforts have been done to apply CFD analysis by Fischer et al. [3], Smith et al. [4], Raza and Kim [5], and Hamman et al. [6] who study 7-pin and 19-pin configuration.

3.1 Pressure Drop Correlations

Friction factor correlations such as Rehme model [10], Engel et al. model [11], and Cheng and Todreas simplified model [12] are widely used for the wire-wrapped fuel bundle. Each friction factor is calculated by the following correlations.

- Rehme model

$$f = \frac{64}{\mathrm{Re}} \cdot F^{0.5} + \frac{0.0816}{\mathrm{Re}^{0.1333}} \cdot \frac{N_r \cdot \pi \cdot \left(D_r + D_w \right)}{S_t} \tag{1}$$

$$\text{Where: } F = \left(\frac{P_t}{D_r} \right)^{0.5} + \left[7.6 \cdot \frac{D_r + D_w}{H} \cdot \left(\frac{P_t}{D_r} \right)^2 \right]$$

- Engel, Markley and Bishop model

$$\begin{aligned} &\text{Laminar flow: } f = \frac{110}{\mathrm{Re}} \text{ for } \mathrm{Re} \le 400, \\ &\text{Turbulent flow: } f = \frac{0.55}{\mathrm{Re}^{0.25}} \text{ for } \mathrm{Re} \ge 5000, \\ &\text{Transition flow: } f = \frac{110}{\mathrm{Re}} \cdot \left(1\text{-}\psi \right)^{0.5} + \frac{0.55}{\mathrm{Re}^{0.25}} \cdot \psi^{0.5} \\ &\qquad\qquad \text{for } 400 \le \mathrm{Re} \le 5000, \\ &\text{Where: } \psi = \frac{(\mathrm{Re} - 400)}{4600\,\mathrm{Re}} \end{aligned} \tag{2}$$

- Cheng and Todreas simplified model

$$\begin{aligned} &\text{Laminar flow: } f = \frac{C_{fL}}{\mathrm{Re}} \text{ for } \mathrm{Re} \le \mathrm{Re}_L, \\ &\text{Turbulent flow: } f = \frac{C_{fT}}{\mathrm{Re}^{0.18}} \text{ for } \mathrm{Re}_\mathrm{T} \le \mathrm{Re}, \\ &\text{Transition flow: } f = \frac{C_{fL}}{\mathrm{Re}} \cdot \left(1\text{-}\psi \right)^{1/3} + \frac{C_{fT}}{\mathrm{Re}^{0.18}} \cdot \psi^{1/3} \\ &\qquad\qquad \text{for } \mathrm{Re}_\mathrm{L} \le \mathrm{Re} \le \mathrm{Re}_\mathrm{T}, \\ &\text{Where: } \log \frac{\mathrm{Re}_L}{300} = 1.7 \cdot \left(\frac{P_t}{D_r} - 1.0 \right), \\ &\log \frac{\mathrm{Re}_T}{10000} = 0.7 \cdot \left(\frac{P_t}{D_r} - 1.0 \right), \\ &\psi = \left(\log \mathrm{Re} - \left(1.7 \cdot \frac{P_t}{D_r} + 0.78 \right) \right) \Big/ \left(2.52 - \frac{P_t}{D_r} \right) \\ &C_{fL} = \left(-974.6 + 1612.0 \cdot \left(\frac{P_t}{D_r} \right) - 598.5 \cdot \left(\frac{P_t}{D_r} \right)^2 \right) \\ &\qquad \cdot \left(\frac{H}{D_r + D_w} \right)^{0.06 - 0.085 \cdot P_t / D_r} \end{aligned} \tag{3}$$

$$C_{fT} = \left\{ \begin{array}{l} 0.8063 - 0.9022 \cdot \log\left(\frac{H}{D_r + D_w}\right) \\ +0.3526 \cdot \left(\log\left(\frac{H}{D_r + D_w}\right)\right)^2 \end{array} \right\} \cdot \left(\frac{P_t}{D_r}\right)^{9.7} \cdot \left(\frac{H}{D_r + D_w}\right)^{1.78 - 2 \cdot P_t/D_r}$$

Bubelis et al. [13] recommend that the Rehme friction factor correlation should be used in the thermal-hydraulic evaluations in the estimation of the pressure drops in wire-wrapped rod/fuel bundles for all reactor types.

3.2 7-Pin Fuel Assembly Simulation Results of PNC

The present investigation of CFD was carried out over the full scale experimental facility of SIENA's 7-pin fuel assembly. Fig. 10 shows the test section of numerical analysis. As shown in Fig. 10, the test section of the CFD analysis is also composed with the heated section of 450mm.

Fig. 11 shows the comparison of the CFD analysis results with friction factor correlations of the Rehme model, Engel et al. model, and Cheng and Todreas simplified model in various Reynolds number range. As you shown in Fig. 11, the Rehme model and Cheng and Todreas model have a good agreement with the CFD analysis results of the 7-pin wire wrapped bundles. Fig. 12 shows the axially distributed friction factors. As shown in Fig. 12, the friction factor near the inlet region is also over-estimated until the inlet flow reaches to about the end of thirdly periodical wire lead pitch position.

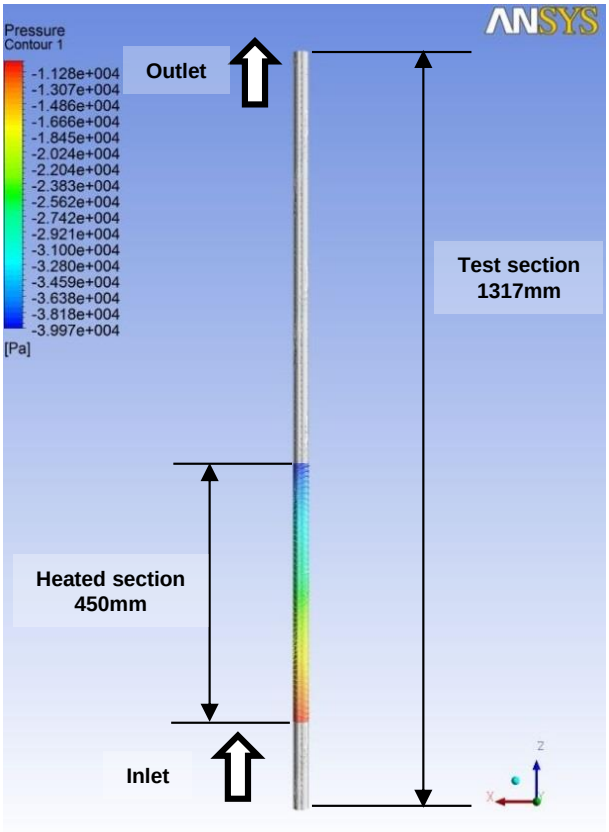

Fig. 10. Numerical test section and duct wall pressure distribution of wire wrapped 7-pin fuel assembly

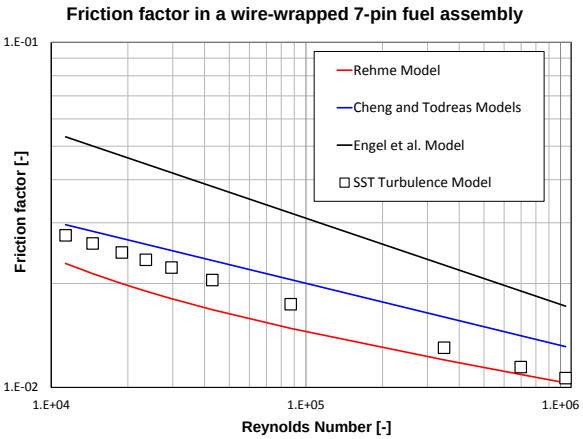

Fig. 11. Comparison of the 7-pin fuel assembly CFD analysis results with friction factor correlations

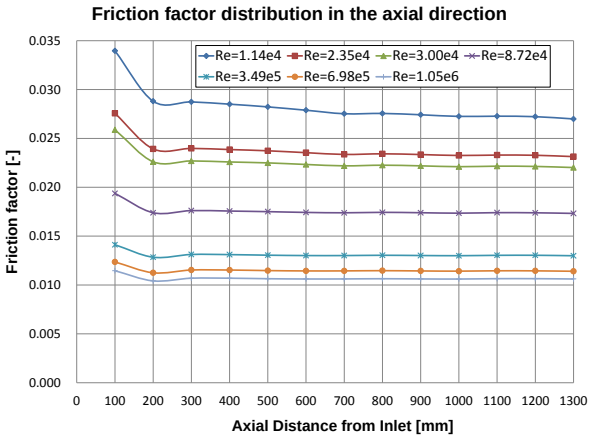

Fig. 12. Axial friction factor distribution

Thermal hydraulic flow field in Reynolds number of 4.29×10^4 has been qualitatively investigated in the 7-pin fuel bundles. Fig. 13 shows the pressure distribution with the local range contour at the wire angular position of 0deg, 90deg, and 180deg. Fig. 14, 15, and 16 the axial velocity, tangential velocity, and temperature distribution normalized by the inlet velocity and the inlet temperature on the cross sectional planes at the wire angular position of 0deg, 90deg, and 180deg. As the wire is helically wrapped in the axial direction, the pressure, axial velocity, tangential velocity, and temperature distribution on the planes is also helically formed with same period of the wire lead pitch in Fig. 13, 14, 15, and 16. Even though the axial velocity on the local area in the opposite direction of the wire dramatically decreases, the tangential velocity on the same area unchanged in Fig. 13 and 14. The temperature distribution is very similar with the axial velocity distribution. The secondary flow cannot dominate the temperature because the axial velocity is much faster than the tangential velocity.

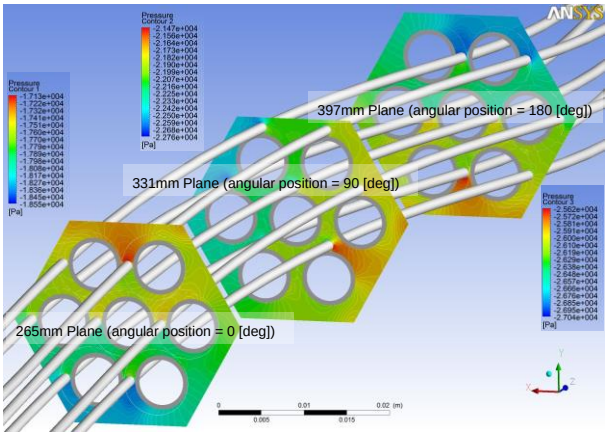

Fig. 13. Pressure distribution with local range contour

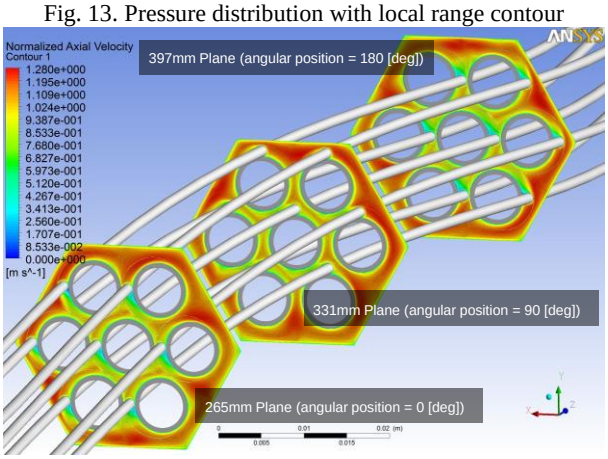

Fig. 14. Normalized axial velocity distribution

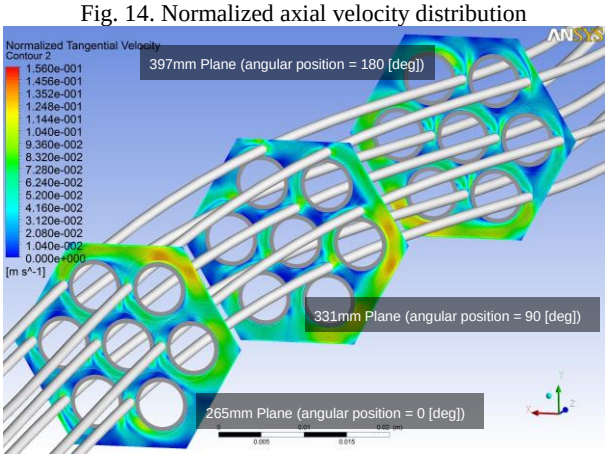

Fig. 15. Normalized tangential velocity distribution

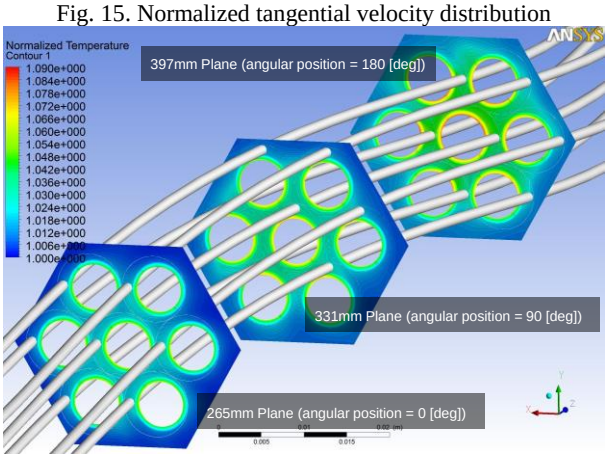

Fig. 16. Normalized temperature distribution

3.3 37-Pin Fuel Assembly Simulation Results of JNC

The present CFD investigation was implemented over the full scale experimental facility of SIENA's 37-pin fuel assembly. Fig. 17 shows the test section of the numerical analysis and pressure distribution on the heated location of the hexagonal duct wall surface. As shown in Fig. 17, the pressure distribution of the heated test section has a helically periodic pattern which has same length of the wire spacer lead pitch. The present numerical investigation is not considering the partial porous blockage state.

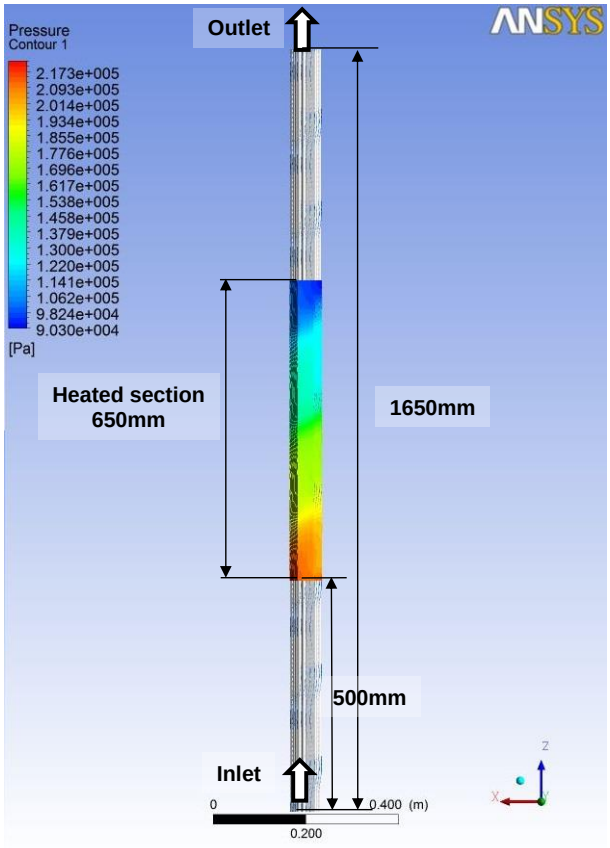

Fig. 17. Numerical test section and duct wall pressure distribution of wire wrapped 37-pin fuel assembly

Fig. 18 shows the comparison of the CFD analysis results with the friction factor correlations of the Rehme model, Engel et al. model, and Cheng and Todreas simplified model in various Reynolds number range. As you shown in Fig. 18, the Rehme model and Engel et al. model agree rather well with the CFD analysis results of the 37-pin fuel assembly. However, in case of the wire wrapped 7-pin fuel bundles, the Rehme model and Cheng and Todreas simplified model have a good agreement with the CFD analysis results of the 7-pin fuel assembly. Fig. 19 shows the axially distributed friction factors. As shown in Fig. 19, the friction factor around the inlet region is also over-estimated until the inlet flow reaches to about the end position of thirdly periodical wire lead pitch.

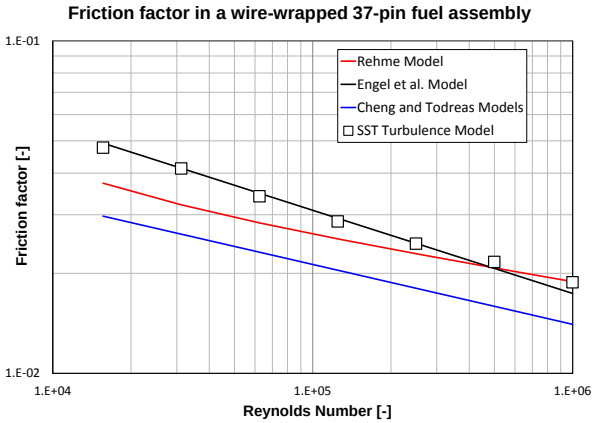

Fig. 18. Comparison of the 37-pin fuel assembly CFD analysis results with friction factor correlations

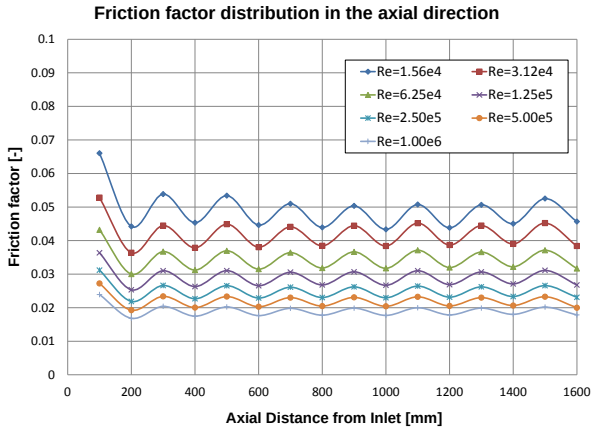

Fig. 19. Axial friction factor distribution

Three-dimensional flow field in Reynolds number of 6.24×10^4 has been investigated in this chapter. Fig. 20 shows the local contour pressure distribution and surface streamline on the planes which are perpendicular to the axial direction and are view from the inlet. Fig. 20 (a), (b), and (c) are the CFD analysis results on the 850mm, 900mm, and 950mm, respectively. As shown in Fig. 20 (a), (b), and (c), large-scale vortex structures between the hexagonal duct wall and the wire-wrapped bundle are developing in the clockwise direction along the axial direction. As the wires are helically wrapped along the axial direction, they have the relative position with the stationary hexagonal duct wall. The relative position would be closely related to the vortex structure behavior and three-dimensional flow phenomena.

Fig. 21 shows the surface streamline on the cross sectional planes of 850 mm, 875mm, 900mm, 925mm, and 950mm. As shown in Fig. 21, the multi-scale vortex structures are developing in the fuel assembly sub-channel. The vortical and separated flow field is composed of the corner vortex structures (yellow dot-line) in the corner sub-channels, the edge vortex structures (white dot-line) in the edge sub-channels, and the interior vortex structures (red dot-line) in the interior vortex sub-channels. The location of the corner and edge vortex structures is closely related with the relative position between the wire and the duct wall. As shown in Fig. 21, the corner and edge vortex structures are developed in the tangential direction when the distance from the wire become far from the duct wall.

Fig. 22 shows the axial and tangential velocity distribution and surface streamline on the cross sectional planes. As shown in Fig. 22 (a), the edge and interior sub-channels has a high axial velocity, and the corner has a low axial velocity. This means that the blockage due to the edge and interior vortex structures are not occurred in the axial direction, however, the corner vortex structures partially induce the axially developed blockage. These strong longitudinal vortex

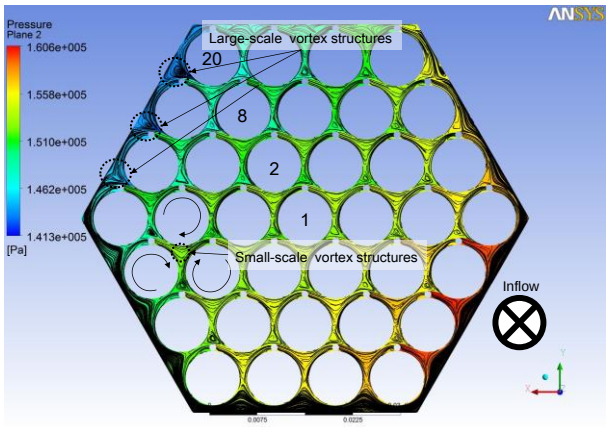

(a) 850mm position from upstream view

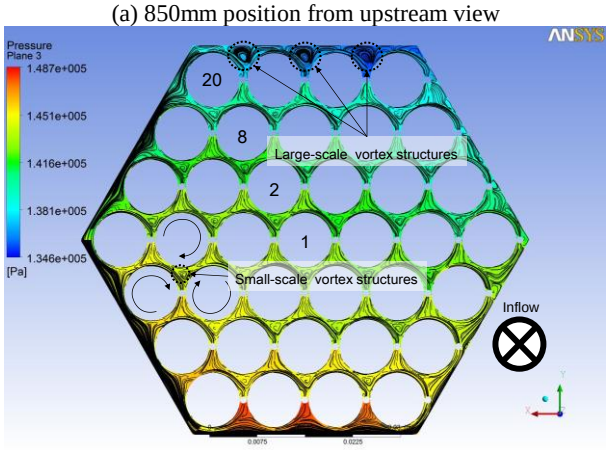

(b) 900mm position from upstream view

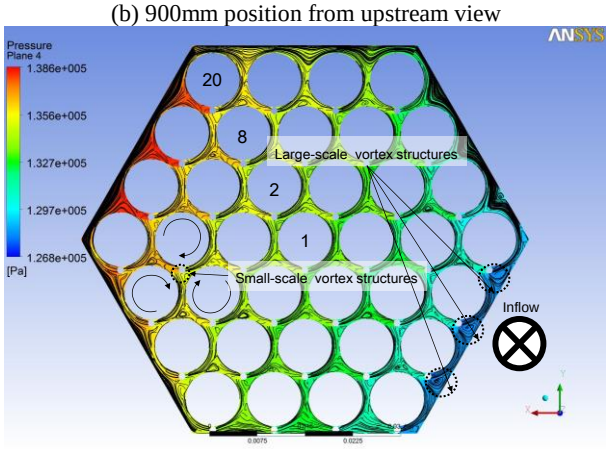

(c) 950mm position from upstream view

Fig. 20. Local contour pressure distribution and surface streamline on the planes

structures in the edge and interior sub-channels can achieve better heat transfer characteristics than that in the corner sub-channels. Furthermore, the wire spacers induce the secondary flow by up to about 13 % of the axial velocity magnitude. The secondary flow in the corner and edge sub-channels is much stronger than that in the interior sub-channel as shown in Fig. 22 (a) and (b).

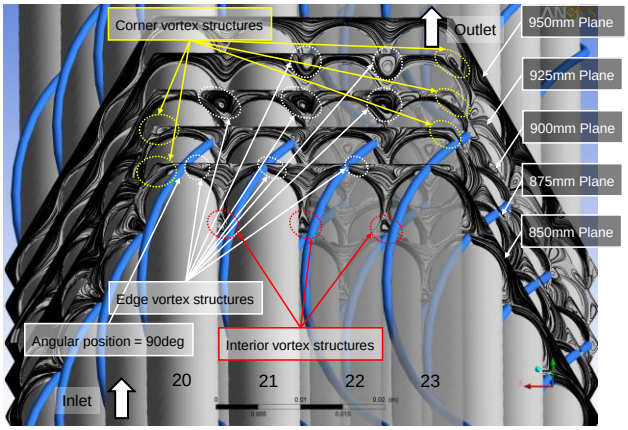

Fig. 21 Surface streamline on the cross sectional planes

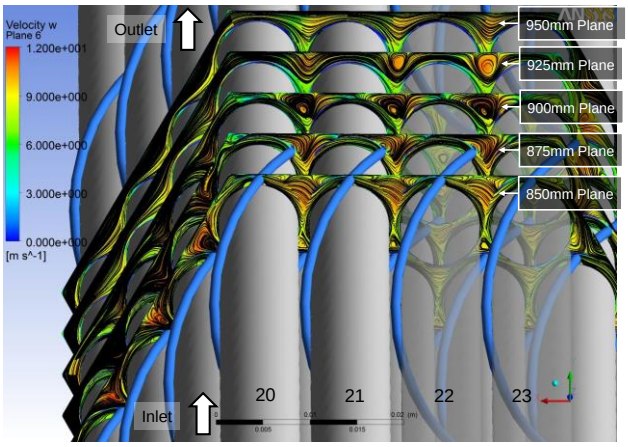

(a) Axial velocity distribution

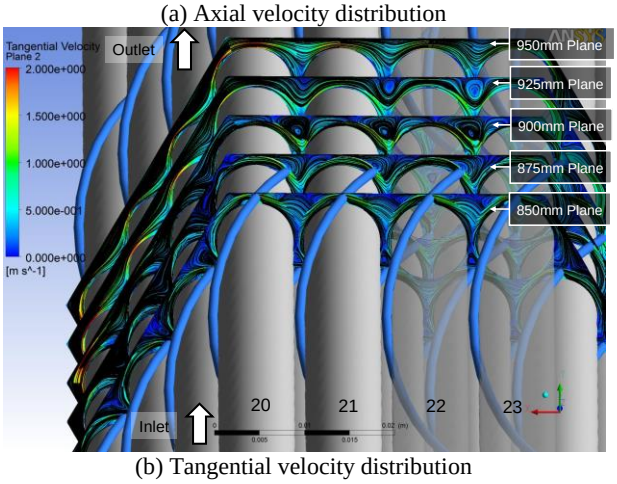

(b) Tangential velocity distribution

Fig. 22. Velocity distribution and surface streamline on the cross sectional planes in the 37-pin fuel assembly

Based on the Biot-Savart law to understand the potential flow, the edge vortex behavior can be explained by the interaction with the edge vortex and the duct wall, as shown in Fig. 23. The induced velocity of the edge vortex by its mirror image acts on the edge vortex in opposite direction of the secondary flow by the wire spacers. For this reason, the edge vortex structures do not shift to the adjacent sub-channel even though the strong secondary flow acts on the edge vortex structures.

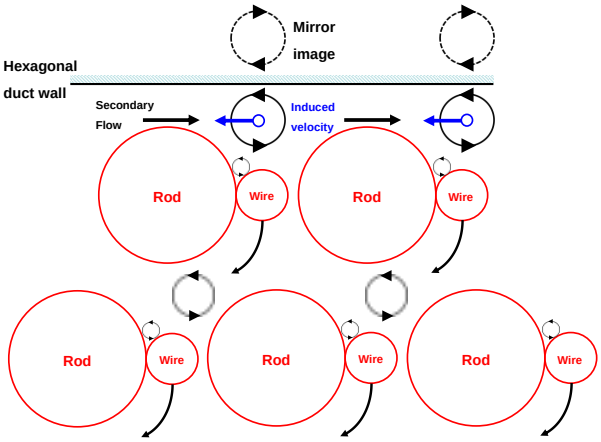

Fig. 23. Potential flow schematic in the edge and interior sub-channel

3.4 217-Pin Fuel Assembly Simulation Results of KAERI 2014 PGSFR

The present investigation of CFD was carried out over the heated section area of the 2014 PGSFR 217-pin fuel assembly designed by the SFR design division of KAERI. Fig. 24 describes the numerical test section and wire-wrapped bundle wall pressure distribution in the 217-pin fuel assembly. As shown in Fig. 24, the 217-pin fuel assembly is fully calculated by the RANS based simulation with SST turbulence model.

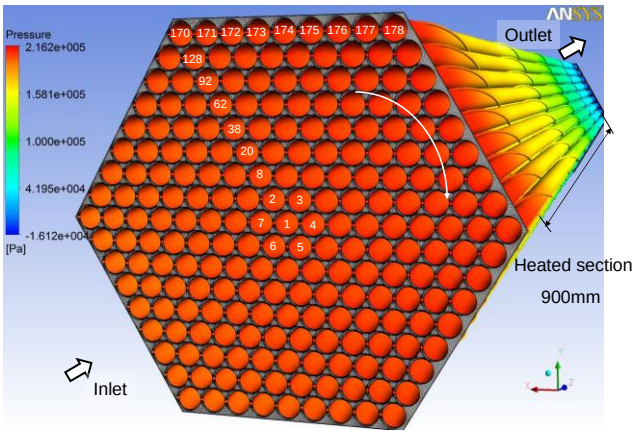

Fig. 24. Numerical test section and bundle wall pressure distribution of wire wrapped 217-pin fuel assembly

Fig. 25 shows the comparison of the 217-pin fuel assembly CFD analysis results with the friction factor correlations of the Rehme model, Engel et al. model, and Cheng and Todreas simplified model in various Reynolds number range. As you shown in Fig. 25, the

Cheng and Todreas model agree rather well with the CFD analysis results of the 217-pin fuel assembly. Fig. 26 shows the axially distributed friction factors. As shown in Fig. 26, the friction factor near the inlet region is also over-estimated until the inlet flow reaches to about the end of thirdly periodical wire lead pitch position.

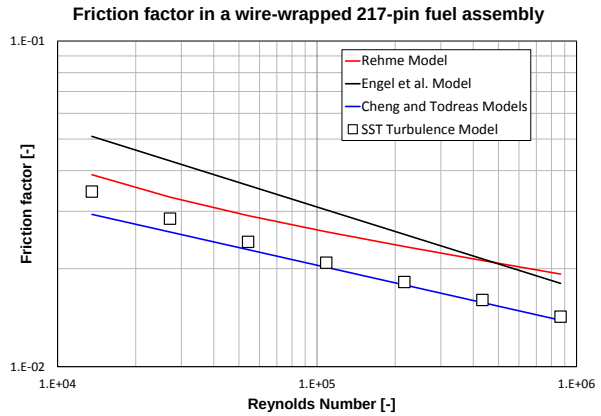

Fig. 25. Comparison of the 217-pin fuel assembly CFD analysis results with friction factor correlations

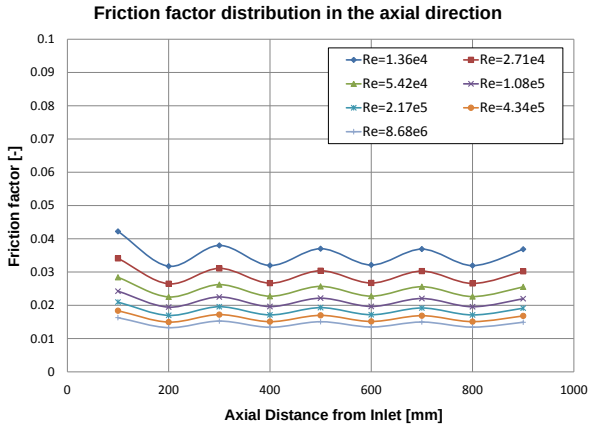

Fig. 26. Axial friction factor distribution

Three-dimensional flow field in Reynolds number of 5.24×10^4 has been investigated in this chapter. Fig. 27 shows the axial and tangential velocity distribution and surface streamline on the cross sectional planes of 650 mm, 675mm, 700mm, 725mm, and 750mm. As shown in Fig. 27 (a), the behavior of the vortex structures in the 217-pin wire-wrapped fuel bundles is same as that in the 37-pin wire-wrapped fuel bundles. The edge and cross sectional planes in the 217-pin fuel assembly interior sub-channels has a high axial velocity, and the corner has a low axial velocity. This phenomenon, which is also same with the 37-pin fuel assembly flow field, means that the axially developed blockage due to the edge and interior vortex structures are not occurred, however, the corner vortex structures partially induce the flow blockage in the axial direction. These strong longitudinal vortex structures in the edge and interior sub-channels can also achieve better heat transfer characteristics than that in the corner sub-channels. Furthermore, the wire spacers induce the secondary flow by up to about 20 % of the axial velocity magnitude. The secondary flow in the corner and edge sub-channels is much stronger than that in the interior sub-channel as shown in Fig. 27 (a) and (b).

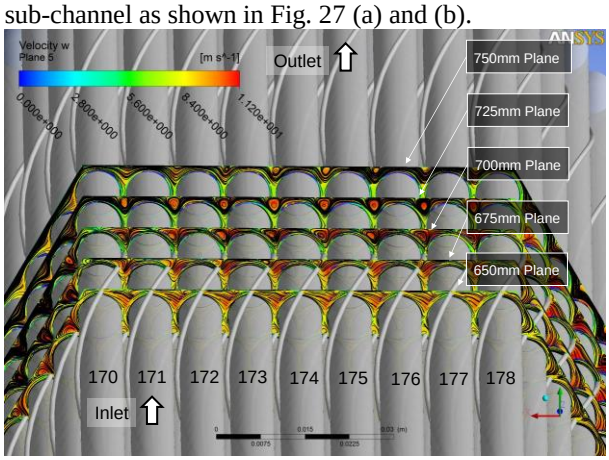

(a) Axial velocity distribution

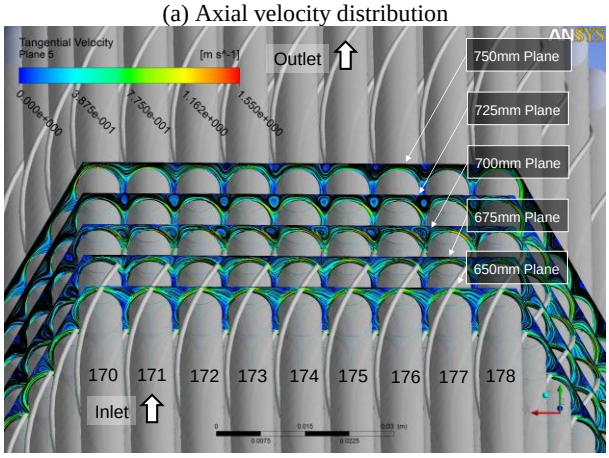

(b) Tangential velocity distribution

Fig. 27. Velocity distribution and surface streamline on the

4. Conclusion

The RANS-based CFD methodology using the innovative hexagonal grid generation with the in-house code and the GGI function of the CFX code has been evaluated in the 7-pin, 37-pin, and 217-pin wire-wrapped fuel assembly. The innovative RANS-based CFD methodology can remarkably reduce the number of meshes. Grid sensitivity study of the wall y* grid scale with SST turbulence model in 7-pin fuel assembly has been carried out, and the uncertainty of friction factor was under the 6.0%. It has been validated that the GGI function of CFX code is very conservative interpolation function. The innovative RANS based CFD methodology can be successfully extended to real 217-pin wire-wrapped fuel assembly of KAERI 2014 PGSFR. The knowledge obtained from the innovative RANS based CFD methodology will contribute to the PGSFR design of KAERI.

ACKNOWLEDGEMENTS

This work has been performed under the nuclear R&D

program supported by the Ministry of Science, ICT and Future Planning of the Republic of Korea.

REFERENCES

[1] Y. Daigo, et al., Local Temperature Rise due to a 6-Channel Blockage in a 7-Pin Bundle, *JAPFNR-202*, 1975.
[2] T. Iitsuka, et al., Study for Subassembly Porous Blockage in Fast Breeder Reactors - Pre-Sub-channel Analysis of 37-Pin Bundle Sodium Test - , *PNC TN9410 98-022*, 1998.
[3] P. F. Fischer, J. Lottes, A. Siegel, and P. Palmiotti, Large Eddy Simulation Of Wire-Wrapped Fuel Pins Ⅰ: Hydrodynamics in a Periodic Array, *Proc. Of M&C +SNA 2007, Monterey, California*, 2007.
[4] J. G. Smith, W. D. Pointer, P. Fischer, B. Babbin, Effects of Mesh Density and Flow Conditioning in Simulating 7-Pin Wire Wrapped Fuel Pins, *Proc. Of ICONE 16, Orlando, FL*, 2008.
[5] W. Raza, K. -Y. Kim, Shape optimization of wire-wrapped 7-pin fuel bundle assembly using Kringing metamodeling technique, *Nuclear Engineering and Design*, 238, pp. 1332-1341, 2008.
[6] K. D. Hamman,, R. A. Berry, R. C. Martineau, and D. Knoll, CFD Sensitivity Analysis of a Fast Reactor Assembly, *Transactions of the American Nuclear Society*, 98, Anaheim, California, 2008.
[7] J. Smagorinsky, General Circulation Experiments with the Primitive Equations. I. The Basic Experiment, *Mon. Weather Rev.*, 91, pp. 99-165, 1963.
[8] D. C. Wilcox, Reassessment of the Scale-determining Equation for Advanced Turbulence Models, *AIAA Journal*, 26(11), pp.1299-1310, 1998.
[9] F. R. Menter, Two-equation eddy-viscosity turbulence models for engineering applications, *AIAA Journal*, 32(8), pp. 1598-1605, 1994.
[10] K. Rehme, Pressure Drop Correlations for Fuel Element Spacers, *Nuclear Technology*, **17**, pp. 15-23, 1973.
[11] F. C. Engel, R. A. Markley, and A. A. Bishop, Laminar, Transition, and Turbulent Parallel Flow Pressure Drop Across Wire-wrap-spaced Rod Bundles, *Nuclear science and engineering*, **69**, pp. 290-296, 1979.
[12] S. K. Cheng and N. E. Todreas, Hydrodynamic Models and Correlations for Bara and Wire-wrapped Hexagonal Rod Bundles-bundle Friction Factors, Sub-channel Friction Factors and Mixing Parameters, *Nuclear Engineering and Design*, **92**, pp. 227-251, 1986.
[13] H. Bubelis and M. Schikorr, Review and Proposal for Best-fit of Wire-wrapped Fuel Bundle Friction Factor and Pressure Drop Predictions Using Various Existing Correlations, *Mitglied der Hermann von Helmholtz-Gemeinschaft Deutscher Forschungs-zentren (HGF)*, ISSN 0947-8620, 2008.